



CHORUS

This is the accepted manuscript made available via CHORUS. The article has been published as:

Hot fusion-evaporation cross sections of ^{44}Ca -induced reactions with lanthanide targets

T. A. Werke, D. A. Mayorov, M. C. Alfonso, E. E. Tereshatov, and C. M. Folden, III

Phys. Rev. C **92**, 054617 — Published 25 November 2015

DOI: [10.1103/PhysRevC.92.054617](https://doi.org/10.1103/PhysRevC.92.054617)

Hot Fusion-Evaporation Cross Sections of ^{44}Ca -Induced Reactions with Lanthanide Targets

T. A. Werke,^{1,2} D. A. Mayorov,^{1,2} M. C. Alfonso,^{1,2} E. E. Tereshatov,¹ and C. M. Folden III^{1, □}

¹*Cyclotron Institute, Texas A&M University, College Station, Texas 77843, USA*

²*Department of Chemistry, Texas A&M University, College Station, Texas 77843, USA*

Background: Previously reported cross sections of ^{45}Sc -induced reactions with lanthanide targets are much smaller than ^{48}Ca -induced reactions on the same targets. ^{44}Ca is one proton removed from ^{45}Sc and could be used to produce nuclei with a relative neutron content between those produced in the ^{45}Sc - and ^{48}Ca -induced reactions.

Purpose: As part of a systematic investigation of fusion-evaporation reactions, cross sections of ^{44}Ca -induced reactions on lanthanide targets were measured. These results are compared to available data for ^{48}Ca - and ^{45}Sc -induced fusion-evaporation cross sections on the same lanthanide targets. Collectively, these data provide insight into the importance of the survival against fission of excited compound nuclei produced near spherical shell closures.

Methods: A beam of $^{44}\text{Ca}^{6+}$ at an energy of ≈ 5 MeV/u was delivered by the K500 superconducting cyclotron at the Cyclotron Institute at Texas A&M University. The desired evaporation residues were selected by the Momentum Achromat Recoil Spectrometer and identified via their characteristic α -decay energies. Excitation functions for the $^{44}\text{Ca} + ^{158}\text{Gd}$, ^{159}Tb , and ^{162}Dy reactions were measured at five or more energies each. A theoretical model was employed to study the fusion-evaporation process.

Results: The ^{44}Ca -induced reactions have xn cross sections that are two orders of magnitude larger than ^{45}Sc -induced reactions, but two orders of magnitude smaller than ^{48}Ca -induced reactions on the same targets. Proton emission competes effectively with neutron emission for the $^{44}\text{Ca} + ^{159}\text{Tb}$ and ^{162}Dy reactions. The maximum $4n$ cross sections in the $^{44}\text{Ca} + ^{158}\text{Gd}$, ^{159}Tb , and ^{162}Dy reactions were 2100 ± 230 , 230 ± 20 , and 130 ± 20 μb , respectively. The $^{44}\text{Ca} + ^{158}\text{Gd}$ and ^{159}Tb cross sections are in good agreement with the respective cross bombardments of $^{48}\text{Ca} + ^{154}\text{Gd}$ and $^{45}\text{Sc} + ^{158}\text{Gd}$ once differences in capture cross sections and compound nucleus formation probabilities are corrected for.

Conclusions: Excitation functions were measured in ^{44}Ca -induced reactions on lanthanide targets. Evaporation residue cross sections were two orders of magnitude larger than ^{45}Sc -induced reactions on the same targets due to an increase in the survival probability of the compound nucleus. However, little evidence of cross section enhancement due to shell stabilization of the compound nucleus was observed.

PACS number(s): 24.60.Dr, 25.70.Gh, 25.70.Jj

□: Corresponding author, email: Folden@comp.tamu.edu

I. Introduction

The area northwest of the $N = 126$, $Z = 82$ shell presents an interesting region to study the various phenomena that contribute to evaporation residue (EvR) production cross sections. Nuclei in this region have a wide range of deformations, level densities, fission barriers, and nucleon separation energies. Previously, we have reported results using ^{48}Ca [1], ^{50}Ti [2], ^{54}Cr [2] and ^{45}Sc [3] projectiles, respectively, to bombard lanthanide targets and produce compound nuclei (CN) with $Z = 84-90$. EvR cross sections for xn exit channels ranged over four orders of magnitude for these reactions, and theoretical modeling emphasized the role of the neutron separation energy and the fission barrier in determining the magnitude of these cross sections. Additionally, it was found that collective enhancements to level density [4] (CELD, also called collective effects) were important in determining the magnitude of the cross sections by enhancing the fission probability for CN produced near the $N = 126$ spherical closed shell. The contribution of proton emission channels to the total EvR cross section was found to be significant in the ^{45}Sc -, ^{50}Ti -, and ^{54}Cr -induced reactions. These projectiles have been considered for synthesizing superheavy elements (SHEs) with $Z > 118$ near the predicted $N = 184$ spherical closed shell [5, 6], but this observation suggests that the production of these SHEs may further be hindered by proton emission in addition to other experimental challenges [6-9].

Fusion-evaporation reactions that produce CN near the $N = 126$ shell have been previously studied and various models have been used to reproduce the cross sections. Vermeulen *et al.* [10] bombarded lanthanide targets with ^{40}Ar projectiles to produce CN near the $N = 126$ shell, and the analysis showed that EvR calculations best fit the data when shell effects were *not* included. Sahm *et al.* [11] produced similar CN in ^{48}Ca -, ^{86}Kr -, and ^{124}Sn -induced reactions and did not observe cross section enhancement due to the presence of the shell closure. More recent work by Heinz *et al.* has suggested that collective phenomena may indeed play a role in enhancing fission probabilities for electromagnetically excited nuclei near the $N = 126$ shell [12]. Additional evidence has shown that CELD may enhance the nuclear level density as suggested by Roy *et al.* [13] and suppress EvR cross sections in reactions that produce isotopes of Fr studied by Singh *et al.* [14]. Other authors have suggested that collective effects are not

necessary to reproduce EvR cross sections away from the $N = 126$ shell because the effects are weak [15] or because the fission barriers are much smaller than predicted by theory [16]. Additionally, α -particle spectra were poorly reproduced when CELD was considered [17]. It is clear that further investigation into the CELD phenomenon is warranted.

In this work, we present measured EvR cross sections in ^{44}Ca -induced reactions for nuclei northwest of the $N = 126$ shell closure. The CN produced in the ^{44}Ca -induced reactions have large shell corrections which should increase the fission barriers and thus the EvR cross sections. However, the influence of CELD may negate this effect, and the cross section enhancement may not be observed. This effort is part of a systematic study of this region using projectiles with $Z \geq 20$ to bombard lanthanide targets [1-3]. ^{44}Ca ($Z = 20$) has one less proton than ^{45}Sc ($Z = 21$), which was the focus of a recent investigation [3], and both projectiles are $N = 24$ isotones. The CN produced by the ^{44}Ca -induced reactions are more neutron-rich than the CN in the ^{45}Sc -induced reactions on the same targets, which increases the fission barrier relative to the neutron separation energy. The results of this work will provide insight into the strength of this effect on the CN survival probability. The chosen reaction systems with ^{44}Ca projectiles give two cross bombardments with reactions previously studied by our group: $^{48}\text{Ca}+^{154}\text{Gd}$ and $^{45}\text{Sc}+^{158}\text{Gd}$. This permits a survey of the effects of the entrance channel in the selected reactions as the survival probability for the CN within each cross bombardment pair should ideally be very similar given the similar excitation energies and angular momenta. The results will be analyzed with a statistical model to elucidate the most important factors in determining the EvR cross sections.

II. Experimental Methods

The experimental setup was nearly identical to that described in our previous work [3], so only important details and differences are presented here. The beam of $^{44}\text{Ca}^{6+}$ was provided by the K500 superconducting cyclotron at the Cyclotron Institute at Texas A&M University with an energy of ≈ 5 MeV/nucleon. The average beam intensity on target was ≈ 0.3 pA. The ^{44}Ca was purchased from Isoflex USA in the oxide powder form (^{44}CaO , $> 95.50\%$ enriched). The beam bombarded targets of $^{158}\text{Gd}_2\text{O}_3$

(334 $\mu\text{g}/\text{cm}^2$ on 2 μm Ti), ^{159}Tb (479 $\mu\text{g}/\text{cm}^2$, self-supporting) and ^{162}Dy (403 $\mu\text{g}/\text{cm}^2$ on 75 $\mu\text{g}/\text{cm}^2$ $^{\text{nat}}\text{C}$). The $^{158}\text{Gd}_2\text{O}_3$ target was prepared on-site using the molecular deposition of the nitrate salt and baking in air at 200°C to convert the material to the oxide [18, 19]. The ^{159}Tb target was purchased from Microfoils Co., and the ^{162}Dy target was prepared by vacuum deposition on $^{\text{nat}}\text{C}$ at Lawrence Berkeley National Laboratory. The beam dose was monitored by a pair of circularly collimated (1 mm diameter) Si detectors in the beam plane and offset by $\pm 30^\circ$ from the beam axis. A plastic blocker 21.6 mm in length with a 6.35 mm diameter circular opening was placed in front of each Si monitor to reduce the number of unwanted particles entering the detector. The absolute beam dose on target was calibrated by an electron-suppressed Faraday Cup located in the target chamber.

The desired reaction products were physically separated using the Momentum Recoil Achromat Spectrometer (MARS) [20, 21]. Fig. 1 shows a schematic of MARS and highlights the important experimental components. The beam energy for the excitation function measurements was varied using 0 (no degrader), 1.8, 2.25, 2.85, 3.45, 4.5, and 5.1 μm Al degraders. All energy losses were estimated using the SRIM code [22, 23] as implemented in LISE++ [24]. The EvR charge state distribution was estimated in LISE++ using the formulas of Schiwietz and Grande [25]. To improve the signal-to-noise ratio for detecting the EvRs, MARS was tuned to select EvRs that were one charge state higher than the estimated peak of the charge state distribution for all data points reported in this work. Experimental charge-state yields were collected for $^{199}\text{At}^{19+}$ and $^{199}\text{At}^{20+}$ (^{199}At is the $4n$ EvR of the $^{44}\text{Ca} + ^{159}\text{Tb}$ reaction) at $E_{\text{Lab, CoT}} = 196.3$ MeV. The yields for $^{199}\text{At}^{19+}$ (the most probable charge state) and $^{199}\text{At}^{20+}$ were compared to the charge-state yield calculations as stated above. The experimental ratio for the yield of $^{199}\text{At}^{20+}/^{199}\text{At}^{19+}$ was 0.94 ± 0.19 , and the calculated ratio was 0.91. Based on these results being in good agreement, the efficiency of MARS for each data point was corrected for the relative abundance of the selected charge state as compared to the maximum charge state with confidence. The overall average transmission efficiency of MARS was estimated to be $(2.3 \pm 0.6)\%$, $(2.3 \pm 0.6)\%$, and $(2.2 \pm 0.5)\%$ for the $^{44}\text{Ca} + ^{158}\text{Gd}$, ^{159}Tb , and ^{162}Dy reactions, respectively via a linear interpolation of the mass asymmetry parameter

from the $^{40}\text{Ar} + ^{116}\text{Sn}$, ^{165}Ho reactions which were previously studied with MARS [1, 21]. Products were tuned to the focal plane of MARS and implanted in a 16-strip Micron Semiconductor model X1 position-sensitive silicon strip detector (PSSD), where they subsequently α -decayed. The fraction of the EvR distribution which implanted into the PSSD was estimated to be $\approx(100 \pm 2)\%$ in the horizontal plane and $\approx(95 \pm 5)\%$ in the vertical plane. A microchannel plate (MCP) detector was positioned in the detector chamber below the beam axis. The heavy recoils passed through a $2\ \mu\text{m}^{\text{nat}}\text{Ti}$ foil and created secondary electrons. The secondary electrons were steered onto the MCP detector via an electrostatic mesh with $\approx 85\%$ transmission efficiency. Coincident signals in the PSSD and MCP detector were classified as heavy recoil events, while a signal only in the PSSD was classified as an α -decay event.

III. Data Analysis and Results

EvR production cross sections for the $^{44}\text{Ca} + ^{158}\text{Gd}$, ^{159}Tb , and ^{162}Dy reactions are presented here for the first time to the best of the authors' knowledge. Relevant properties of the three reactions and the resulting CN are presented in Table I. The beam energy was selected to maximize production of the $4n$ EvR as is common in a "warm fusion" experiment. Decay properties of the $4n$ and $p3n$ EvRs are presented in Table II. The experiment was only sensitive to the α -decaying exit channels, and EvRs were uniquely identified by their characteristic α -energies. Examples of the raw α -decay spectra (events discriminated as α particles by the MCP veto detector) are presented in Fig. 2. The raw α -decay spectra were fit using the GF3 program that is part of the RADWARE package [26]. Due to low statistics for some exit channels caused by small α -branching ratios or small cross sections, a simple statistical test identical to that described in Ref. [27] and Eq. (1) in Ref. [3] was then performed to determine if the number of data counts in the peak was above background. Regions of interest (ROIs) were identified for each of the possible reaction products based on the PSSD resolution, and a flat background was fit to each spectrum to determine the number of background counts per bin. The number of background counts was determined for each ROI and was assumed to follow a Poisson distribution. If the number of counts

observed in the data peak was greater than or equal to the 95% upper limit of a cumulative Poisson distribution of background counts, then the peak was accepted to be a real EvR peak. Once a peak was determined to be above background, the background number of counts in the ROI was subtracted from the observed number of counts in the alpha spectrum to determine the EvR cross section. Additionally, it was possible to correlate xn EvR implant events with α -decays for the $4n$ EvRs of the $^{44}\text{Ca} + ^{159}\text{Tb}$ and ^{162}Dy reactions due to good EvR statistics, low backgrounds, and short α -decay half-lives. Decay times for EvR- α_1 events for these reactions are presented in panels (a) and (b) of Fig. 3. The EvR- α_1 correlation search was constrained to events occurring in the same strip of the PSSD strip (≈ 3 mm width) and within a ± 1.5 mm vertical position window. Position differences for EvR- α_1 correlations are presented in Fig. 3(c). The maximum allowable time, Δt_{max} , was set to five half-lives of the decaying nucleus. The experimental lifetimes of the decaying nuclides were extracted by fitting with the exponential function described by Eq. (8) in Ref. [28] and were compared with literature values taken from Ref. [29]. EvR- α_1 - α_2 correlations were observed for the $^{44}\text{Ca} + ^{162}\text{Dy}$ reaction, and correlations for the peak of the $4n$ excitation function ($E_{\text{Lab, CoT}} = 188.9$ MeV) are presented in Fig. 3(d). Based on the α -detection probability of the detector of $\approx (55 \pm 3)\%$ and the α -branching ratio of the $4n$ EvR [^{202}Rn , α -branching ratio = $(78 \pm 8)\%$], it is expected that 39 observed $4n$ EvR- α decays would result in ≈ 17 observed EvR- α_1 - α_2 decays. Therefore, the observation of 13 events in Fig. 3(d) is reasonable.

Many xn EvR cross sections were measured for all three reactions, and pxn cross sections were measured for the $^{44}\text{Ca} + ^{159}\text{Tb}$ and ^{162}Dy reactions. No pxn channels were observed in the $^{44}\text{Ca} + ^{158}\text{Gd}$ reaction due to the low α -branching ratios of the pxn products ($< 1\%$ for all channels). No α or αxn exit channels were observed in any of the reactions. A full listing of cross sections for all observed exit channels is reported in Table III. All reported error bars are calculated at the 1σ level according to Ref. [27]. Asymmetric error bars are reported for cases of small statistics (< 30 observed EvR counts in the peak). All associated errors are statistical only, and absolute errors are estimated to be $\pm 50\%$ primarily due to uncertainties in the transmission efficiency of MARS.

In this work, we compare the xn and pxn cross sections of the ^{44}Ca -induced reactions with the ^{48}Ca - and ^{45}Sc -induced reactions on the same targets. Moreover, the ^{44}Ca reaction data are evaluated against available ^{48}Ca - and ^{45}Sc -induced cross bombardment data. The data for the $4n$ and $p3n$ exit channels of the ^{44}Ca -induced reactions measured in the current work are plotted in Fig. 4, and comparisons of the $4n$ cross sections with ^{48}Ca - and ^{45}Sc -induced reactions [1, 3] are presented in Fig. 5. Although ^{44}Ca is only one proton removed from ^{45}Sc , the xn cross sections in the ^{44}Ca -induced reactions are up to two orders of magnitude larger than in the ^{45}Sc -induced reactions. The maximum $4n$ cross sections for the $^{44}\text{Ca} + ^{158}\text{Gd}$, ^{159}Tb , and ^{162}Dy reactions are factors of 54 ± 11 , 96_{-57}^{+92} , and 72 ± 26 *larger* than the respective ^{45}Sc -induced reactions on the same targets. Additionally, the maximum pxn cross sections in the ^{44}Ca -induced reactions are a factor of 5-10 larger than the maximum pxn cross sections in the ^{45}Sc -induced reactions. However, the maximum $4n$ cross sections in the $^{44}\text{Ca} + ^{159}\text{Tb}$ and ^{162}Dy reactions are factors of 55 ± 9 and 97 ± 20 *smaller* than in the ^{48}Ca -induced reactions on the same targets due to the relative neutron-richness of ^{48}Ca as compared to ^{44}Ca . This leads to CN with lower neutron binding energies and higher fission barriers, which results in larger CN survival probabilities in the ^{48}Ca -induced reactions (see Sec. V for further discussion). No pxn exit channels were observed in any of the ^{48}Ca -induced reactions either due to lack of proton emission from the CN or from small α -branching ratios of the pxn products. However, the sum xn EvR cross sections in the ^{48}Ca -induced reactions are still orders of magnitude larger than the total measured EvR cross sections for ^{44}Ca -induced reactions on the same targets.

The $^{44}\text{Ca} + ^{158}\text{Gd}$ reaction provides a cross bombardment of the $^{48}\text{Ca} + ^{154}\text{Gd}$ reaction previously studied by our group, and the $^{44}\text{Ca} + ^{159}\text{Tb}$ reaction provides a cross bombardment of the $^{45}\text{Sc} + ^{158}\text{Gd}$ reaction. The $4n$ EvR cross sections for the two pairs of cross bombardments are presented in Fig. 6. The $4n$ cross sections measured for the $^{44}\text{Ca} + ^{158}\text{Gd}$ reaction agree well with the $^{48}\text{Ca} + ^{154}\text{Gd}$ cross sections in magnitude even though the Q-value shifts the excitation energy for the ^{48}Ca -induced reaction down by 5.8 MeV relative to the ^{44}Ca -induced reaction. Additionally, no pxn channels were observed in either reaction. Calculations for the capture cross section multiplied by compound nucleus formation probability

(the “entrance channel”, see Sec. IV for details) are shown by the solid lines in Fig. 6 and account for the difference in the $4n$ EvR cross sections between the two reactions (see Sec. V below for discussion). There is also a significant difference in the $4n$ cross sections between the $^{44}\text{Ca} + ^{159}\text{Tb}$ and the $^{45}\text{Sc} + ^{158}\text{Gd}$ reactions. Again, this difference can be attributed primarily to entrance channel effects as shown in Fig. 6. Despite the differences in the entrance channel asymmetries and the Q-values for the cross bombardments, these are only secondary effects in determining the magnitudes of the EvR cross sections.

IV. Theoretical Model

To learn more about the reaction mechanism and to study the most important factors in determining the EvR cross sections, a simple theoretical model was developed. The model used in the present work is identical to that described in our previous publication [3], so only the major components will be discussed here. Evaporation residue cross sections σ_{EvR} are commonly modeled as the product of three factors:

$$\sigma_{\text{EvR}}(E_{\text{cm}}) = \sigma_{\text{capt}}(E_{\text{cm}}) \cdot P_{\text{CN}}(E_{\text{cm}}, l) \cdot W_{\text{sur}}(E_{\text{CN}}^*, l_{\text{CN}}), \quad (1)$$

where σ_{capt} is the capture cross section for the projectile and target to overcome the Coulomb repulsion and enter a “touching spheres” configuration, P_{CN} is the probability that the system then evolves into an equilibrated compound nucleus, and W_{sur} is the probability the excited, rotating compound nucleus survives against fission as it de-excites and reaches the cold evaporation residue. In Eq. (1), E_{cm} is the kinetic energy of the projectile in the center-of-mass frame, l is the angular momentum brought in by the projectile, and l_{CN} is the angular momentum of the compound nucleus, and E_{CN}^* is the total excitation energy of the compound nucleus.

The capture cross section σ_{capt} was calculated using the semi-empirical “diffused barrier formula” developed by Świątecki *et al.* [30], and full details are described by Eqs. (2) through (8) in Ref. [1]. The compound nucleus formation probability is hindered by the quasifission of the hot, rotating dinuclear system into two fission-like fragments. Quasifission has been shown to hinder CN formation in heavy

ion-induced reactions with deformed targets for systems with charge product $Z_p Z_t > 1000$ [31-35], where Z_p is the atomic number of the projectile and Z_t is the atomic number of the product. As shown in Table I, the charge products of the ^{44}Ca -induced reactions are greater than 1000. The quantity P_{CN} is calculated with the method of Siwek-Wilczyńska *et al.* [36] and details are described by Eq. (9) in Ref. [1].

The compound nucleus survival probability is treated within a simple statistical framework. The survival probability is calculated as

$$W_{\text{sur}} = P_{xn}(U_{\text{CN}}) \prod_{j=1}^x (\Gamma_n / \Gamma_{\text{tot}})_j, \quad (2)$$

where $P_{xn}(U_{\text{CN}})$ is the probability of emitting exactly x neutrons given an initial thermal excitation energy U_{CN} , i.e., the ‘‘Jackson Factor’’ [37], Γ_n is the neutron decay width and Γ_{tot} is the sum of the particle decay widths (neutron, proton, and alpha emission were considered for these reactions) and the fission decay width, Γ_f . The survival probability is calculated according to Eqs. (5) through (15) in Ref. [3] and the associated discussion therein.

The inclusion of collective enhancements to the level density (CELD) has been found to be an important component of the model in order to reproduce the magnitude of the experimental data in our previous work [1-3]. As such, the effect is included here following the prescription of Zagrebaev *et al.* [38]:

$$K_{\text{coll},i}(U_i, \beta_2) = [K_{\text{rot},i} \phi(\beta_2) + K_{\text{vib},i} \phi(1 - \beta_2)] f(U_i). \quad (3)$$

$K_{\text{rot},i}$ and $K_{\text{vib},i}$ are the rotational and vibrational enhancement factors, respectively (where i denotes particle emission or fission), the function $\phi(\beta_2)$ is a smoothing function that describes the shape of a nucleus as it undergoes particle emission or fission, and the function $f(U_i)$ is a Fermi function that fades out the strength of CELD as excitation energy increases. Typically, $K_{\text{rot},i}$ (≈ 80 -150) is approximately one order of magnitude larger than $K_{\text{vib},i}$ (≈ 1 -10) due to the smaller spacing of rotational levels. The overall

collective enhancement factor, K_{coll} directly multiplies Γ_i or Γ_f in the survival calculations. Full details of the CELD calculations are described by Eqs. (16) through (20) in Ref. [3].

V. Discussion

Model calculations in this work are reported as solid lines in Fig. 4. The $4n$ calculations agree well with the data, but the $p3n$ calculations are much smaller in magnitude than the data. The model described above was tested against experimental data over four orders of magnitude with satisfactory results in the previous publication [3]. The model calculations in that work generally agreed well with the $4n$ data in both shape and magnitude, but the $p3n$ calculations were also significantly lower than the data. The most likely explanation is that the proton emission barrier was too large even with use of the semi-empirical charged-particle barrier calculations of Parker *et al.* [see Eqs. (8) and (9) in Ref. [39]].

The two cross bombardments in this work provide an opportunity to test how well the model calculates $\sigma_{\text{capt}}P_{\text{CN}}$, as W_{sur} should ideally be nearly identical for each reaction within the cross bombardment pair for similar values of E_{CN}^* and l . The $4n$ cross sections for the cross bombardments are presented in Fig. 6 with calculations for $\sigma_{\text{capt}}P_{\text{CN}}$ (solid lines). The difference in cross section can be fully explained by these changes in $\sigma_{\text{capt}}P_{\text{CN}}$. This is especially evident in the $^{44}\text{Ca} + ^{159}\text{Tb}$ and $^{45}\text{Sc} + ^{158}\text{Gd}$ cross bombardment, where the $4n$ cross sections are almost a whole order of magnitude different. At $E_{\text{CN}}^* \approx 50$ MeV, the difference in the measured $4n$ cross sections is $\sigma_{4n}(^{44}\text{Ca})/\sigma_{4n}(^{45}\text{Sc}) \approx 6.5 \pm 1.2$, and the calculated difference due to the entrance channel is $\sigma_{\text{capt}}P_{\text{CN}}(^{44}\text{Ca})/\sigma_{\text{capt}}P_{\text{CN}}(^{45}\text{Sc}) \approx 6$. The ^{45}Sc data are taken from Table III of Ref. [3], and although there is no data point near $E_{\text{CN}}^* = 50$ MeV for the $^{45}\text{Sc} + ^{158}\text{Gd}$ reaction, a simple linear interpolation was done between the points at $E_{\text{CN}}^* = 47.6$ MeV and 52.2 MeV to estimate the $4n$ cross section at $E_{\text{CN}}^* = 50$ MeV. The error was estimated based on the errors of the surrounding data points. Although P_{CN} has a large error associated with it (up to an order of

magnitude [40]), these results indicate that our approach to calculating P_{CN} leads to good agreement with the data.

The xn cross sections in the ^{44}Ca -induced reactions studied in the current work are two orders of magnitude larger than ^{45}Sc -induced reactions on the same target, but two orders of magnitude smaller than ^{48}Ca -induced reactions on the same targets. This can be seen by comparing Table III in the current work to Table III in Ref. [3] and Table II in Ref. [1]. These combined data are also presented in this work in Fig. 5. The survival probability strongly depends on the neutron separation energy and the fission barrier [6]:

$$W_{\text{sur}} \propto \prod_{j=1}^x \exp[(B_f - S_n)/T]_j . \quad (4)$$

This leads to the following approximation for xn reactions:

$$W_{\text{sur}} \propto \{\exp[\overline{(B_f - S_n)}/T]\}^x , \quad (5)$$

where $\overline{B_f - S_n}$ is the average value of the fission barrier minus the neutron separation energy across the entire deexcitation cascade. The quantity $\overline{B_f - S_n}$ is reported for each of the three reactions studied in this work in Table I. This effect is illustrated in Fig. 7, which shows the peak measured $4n$ cross sections as a function of $\overline{B_f - S_n}$ for fusion reactions with ^{40}Ar [10], ^{44}Ca (this work), ^{48}Ca [1], ^{50}Ti [2], ^{54}Cr [2], and ^{124}Sn [11] projectiles. The maximum $4n$ cross sections for the ^{44}Ca - and ^{50}Ti -induced reactions are almost identical even though the projectiles and the CN produced are very different. As shown in Fig. 7, the values of $\overline{B_f - S_n}$ for the ^{44}Ca - and ^{50}Ti -induced reactions are almost equal as well. Although $\sigma_{\text{capt}}P_{\text{CN}}$ causes some difference in the $4n$ cross sections, $\overline{B_f - S_n}$ is the primary factor in determining the EvR cross sections. As the values of $\overline{B_f - S_n}$ decrease, so do the values of $\sigma_{\text{max}, 4n}$, and this is especially

apparent as the abscissa drops from ≈ 2 MeV to ≈ 0 MeV. This suggests that maximizing $\overline{B_f - S_n}$ is critical to maximizing the EvR cross sections.

The dashed and solid lines on Fig. 7 indicate the maximum of the theoretical calculation for each of the reactions with (dashed line) and without (solid line) CELD. The grey bands above and below each line indicate the same calculations with a ± 0.5 MeV change in B_f (this corresponds to the estimated uncertainty of B_f [41]). These calculations emphasize the impact of CELD in determining W_{sur} ; for all values of $\overline{B_f - S_n}$, the best agreement between theory and experiment occurs when CELD is included. As $\overline{B_f - S_n}$ decreases, there is a sharp decrease in $\sigma_{\text{max}, 4n}$ that is perhaps due the interplay of several effects. The influence of CELD is greater for spherical nuclei than for deformed nuclei due to the absence of rotational levels above the ground state ($K_{\text{rot}} = 1$). However, if $\overline{B_f - S_n}$ is large, then neutron emission dominates because $\Gamma_n \gg \Gamma_f$ and CELD has a weak effect. This is illustrated in Fig. 7, where the difference between the calculations with and without CELD is only *one* order of magnitude or less for large values of $\overline{B_f - S_n}$. For small values of $\overline{B_f - S_n}$, neutron emission no longer dominates and including CELD makes $\Gamma_n < \Gamma_f$, resulting in a *three* order of magnitude difference in the calculations with and without K_{coll} at $\overline{B_f - S_n} \approx 0$ MeV. If this same effect extends to the production of spherical, shell stabilized SHEs near the predicted $N = 184$ closed shell, then the EvR cross sections for those nuclei may not be enhanced due to the shell closure. This experimental work suggests that ^{44}Ca produces CN with higher survival probabilities than ^{45}Sc , but still much smaller than ^{48}Ca . This conclusion is not entirely surprising, and the quantitative data collectively show that the differences in production cross sections for these systems are large.

VI. Conclusions

Excitation functions of the $^{44}\text{Ca} + ^{158}\text{Gd}$, ^{159}Tb , and ^{162}Dy reactions are reported for the first time. The xn cross sections are two orders of magnitude larger than ^{45}Sc -induced reactions on the same targets, but two orders of magnitude smaller than ^{48}Ca -induced reactions on the same targets. Proton emission competes effectively with neutron emission from the CN, and pxn cross sections are similar in magnitude to the xn cross sections. The two cross bombardments are in good agreement once the difference in entrance channel effects are accounted for. A theoretical model was employed to understand the data. The primary factor in determining the xn EvR cross sections is the difference in the fission barrier and the neutron separation energy. Collective effects were necessary to reproduce the EvR cross sections. This suggests that SHE cross sections may not be enhanced due to the predicted spherical shell closure at $N=184$, a conclusion that supports prior reports.

VII. Acknowledgements

The authors would like to thank the accelerator group and technical staff of the Cyclotron Institute for delivering the beams of ^{44}Ca . We also thank the Heavy Elements Group at Lawrence Berkeley National Laboratory for providing the ^{162}Dy target used in these experiments. This material is based upon work supported by the U.S. Department of Energy, Office of Science, Office of Nuclear Physics under Award Numbers DE-FG02-93ER40773, DE-FG02-12ER41869/DE-SC0008126, and DE-FG07-05ID14692/MUSC09-100. Additionally, this work was supported by the Robert A. Welch Foundation under award number A-1710, and the Texas A&M University College of Science.

References

- [1] D. A. Mayorov, T. A. Werke, M. C. Alfonso, M. E. Bennett, and C. M. Folden III, *Phys. Rev. C* **90**, 024602 (2014).
- [2] D. A. Mayorov, T. A. Werke, M. C. Alfonso, E. E. Tereshatov, M. E. Bennett, M. M. Frey, and C. M. Folden III, *Phys. Rev. C* (**submitted**).
- [3] T. A. Werke, D. A. Mayorov, M. C. Alfonso, M. E. Bennett, M. J. DeVanzo, M. M. Frey, E. E. Tereshatov, and C. M. Folden III, *Phys. Rev. C* (**to be published**).
- [4] A. R. Junghans, M. de Jong, H. G. Clerc, A. V. Ignatyuk, G. A. Kudyaev, and K.-H. Schmidt, *Nucl. Phys. A* **629**, 635 (1998).
- [5] J. H. Hamilton, S. Hofmann, and Y. T. Oganessian, *Ann. Rev. Nucl. Part. Sci.* **63**, 383 (2013).
- [6] Y. T. Oganessian and V. K. Utyonkov, *Rep. Prog. Phys.* **78**, 036301 (2015).
- [7] S. Hofmann *et al.*, GSI Scientific Report No. PHN-NUSTAR-SHE-01, edited by K. Große, 2011, p. 205.
- [8] Y. T. Oganessian *et al.*, *Phys. Rev. C* **79**, 024603 (2009).
- [9] Y. T. Oganessian, *J. Phys. G: Nucl. Part. Phys.* **34**, R165 (2007).
- [10] D. Vermeulen, H.-G. Clerc, C.-C. Sahm, K.-H. Schmidt, J. G. Keller, G. Munzenberg, and W. Reisdorf, *Z. Phys. A* **318**, 157 (1984).
- [11] C.-C. Sahm, H.-G. Clerc, K.-H. Schmidt, W. Reisdorf, P. Armbruster, F. P. Hessberger, J. G. Keller, G. Münzenberg, and D. Vermeulen, *Nucl. Phys. A* **441**, 316 (1985).
- [12] A. Heinz *et al.*, *Nucl. Phys. A* **713**, 3 (2003).
- [13] P. Roy *et al.*, *Phys. Rev. C* **88**, 031601(R) (2013).
- [14] V. Singh *et al.*, *Phys. Rev. C* **89**, 024609 (2014).
- [15] K. Siwek-Wilczyńska, I. Skwira, and J. Wilczyński, *Phys. Rev. C* **72**, 034605 (2005).
- [16] R. Sagaidak and A. Andreyev, *Phys. Rev. C* **79**, 054613 (2009).
- [17] S. Komarov, R. J. Charity, C. J. Chiara, W. Reviol, D. G. Sarantites, L. G. Sobotka, A. L. Caraley, M. P. Carpenter, and D. Seweryniak, *Phys. Rev. C* **75**, 064611 (2007).
- [18] W. Parker and R. Falk, *Nucl. Instrum. Methods* **16**, 355 (1962).
- [19] W. Parker, H. Bildstein, N. Getoff, H. Fischer-Colbrie, and H. Regal, *Nucl. Instrum. Methods* **26**, 61 (1964).
- [20] R. E. Tribble, R. H. Burch, and C. A. Gagliardi, *Nucl. Instrum. Methods. Phys. Res., Sect. A* **285**, 441 (1989).
- [21] C. M. Folden III *et al.*, *Nucl. Instrum. Methods. Phys. Res., Sect. A* **678**, 1 (2012).
- [22] J. F. Ziegler *et al.*, *The Stopping and Range of Ions in Solids* (Pergamon, New York, 1984).
- [23] J. F. Ziegler, M. D. Ziegler, and J. P. Biersack, *Nucl. Instrum. Methods. Phys. Res., Sect. B* **268**, 1818 (2010).
- [24] O. Tarasov and D. Bazin, *Nucl. Instrum. Methods. Phys. Res., Sect. B* **266**, 4657 (2008).
- [25] G. Schiwietz and P. L. Grande, *Nucl. Instrum. Methods. Phys. Res., Sect. B* **175**, 125 (2001).
- [26] D. C. Radford, *RADWARE Software Package*; available at <http://radware.phy.ornl.gov>.
- [27] K.-H. Schmidt, C.-C. Sahm, K. Pielenz, and H.-G. Clerc, *Z. Phys. A* **316**, 19 (1984).
- [28] K. H. Schmidt, *Eur. Phys. J. A* **8**, 141 (2000).
- [29] National Nuclear Data Center; available at <http://www.nndc.bnl.gov/chart/>.
- [30] W. Świątecki, K. Siwek-Wilczyńska, and J. Wilczyński, *Phys. Rev. C* **71**, 014602 (2005).
- [31] A. C. Berriman, D. J. Hinde, M. Dasgupta, C. R. Morton, R. D. Butt, and J. O. Newton, *Nature (London)* **413**, 144 (2001).
- [32] D. J. Hinde, M. Dasgupta, J. R. Leigh, J. P. Lestone, J. C. Mein, C. R. Morton, J. O. Newton, and H. Timmers, *Phys. Rev. Lett.* **74**, 1295 (1995).

- [33] E. Prasad *et al.*, Phys. Rev. C **81**, 054608 (2010).
- [34] C. Yadav *et al.*, Phys. Rev. C **86**, 034606 (2012).
- [35] E. Williams *et al.*, Phys. Rev. C **88**, 034611 (2013).
- [36] K. Siwek-Wilczyńska, A. Borowiec, I. Skwira-Chalot, and J. Wilczyński, Int. J. Mod. Phys. E **17**, 12 (2008).
- [37] J. D. Jackson, Can. J. Phys **34**, 767 (1956).
- [38] V. I. Zagrebaev, Y. Aritomo, M. G. Itkis, Yu. Ts. Oganessian, and M. Ohta, Phys. Rev. C **65**, 014607 (2001).
- [39] W. E. Parker *et al.*, Phys. Rev. C **44**, 774 (1991).
- [40] R. Yanez, W. Loveland, J. S. Barrett, L. Yao, B. B. Back, S. Zhu, and T. L. Khoo, Phys. Rev. C **88**, 014606 (2013).
- [41] A. J. Sierk, Computer Code *fisrot*, available at <https://www-nds.iaea.org/RIPL-3/fission/fis-barrier-liquiddrop.for>.
- [42] A. J. Sierk, Phys. Rev. C **33**, 2039 (1986).
- [43] P. Möller, J. R. Nix, W. D. Myers, and W. Świątecki, At. Data Nucl. Data Tables **59**, 185 (1995).

TABLES

TABLE I. Reaction properties of the ^{44}Ca -induced reactions reported in this work. N_{CN} is the neutron number of the compound nucleus. $Z_p Z_t$ is the charge product of the reaction entrance channel. $\overline{B_f - S_n}$ is the average difference of the fission barrier and the neutron separation energy across the de-excitation cascade up to the $4n$ exit channel. Fission barriers in this table are calculated for $l = 0$ using the macroscopic component of Sierk [42] plus the microscopic component of Möller *et al.* [43]. Particle separation energies and associated uncertainties are taken from the National Nuclear Data Center [29]. $\beta_2(\text{CN})$ is the quadrupole deformation parameter of the CN and is also taken from Ref. [29].

Reaction	CN	N_{CN}	$Z_p Z_t$	$\overline{B_f - S_n}$ (MeV)	$S_p(\text{CN})$ (MeV)	$S_n(\text{CN})$ (MeV)	$\beta_2(\text{CN})$
$^{44}\text{Ca} + ^{158}\text{Gd}$	^{202}Po	118	1280	4.1	3.798(21)	9.471(16)	0.009
$^{44}\text{Ca} + ^{159}\text{Tb}$	^{203}At	118	1300	1.8	1.527(18)	9.64(3)	0.045
$^{44}\text{Ca} + ^{162}\text{Dy}$	^{206}Rn	120	1320	1.9	3.434(21)	9.47(5)	-0.044

TABLE II. Measured and reported EvR decay properties of the $4n$ and $p3n$ exit channels of the ^{44}Ca -induced reactions reported in the current work. Ground state decays were not observed for some nuclides, so excited state decays are reported if applicable. $E_{\alpha, \text{obs}}$ (keV) is the measured α -energy obtained by fitting the energy spectra with GF3. Literature values for the α -energy, branching ratio, and half-life are

Reaction	$4n,$ $p3n$ EvRs	$E_{\alpha, \text{obs}}$ (keV)	$E_{\alpha, \text{lit}}$ (keV)	$b_{\alpha, \text{lit}}$ (%)	$t_{1/2, \text{lit}}$
$^{44}\text{Ca} + ^{158}\text{Gd}$	^{198}Po	6158 ± 35	6182 ± 2	57 ± 2	1.77 ± 0.03 min
	^{198}Bi	N/A	N/A	0	10.3 ± 0.3 min
$^{44}\text{Ca} + ^{159}\text{Tb}$	^{199}At	6640 ± 38	6643 ± 3	90 ^a	6.92 ± 0.13 s
	$^{199\text{m}}\text{Po}$	6032 ± 34	6059 ± 3	9.4 ± 1	4.17 ± 0.05 min
$^{44}\text{Ca} + ^{162}\text{Dy}$	^{202}Rn	6618 ± 27	6639.5 ± 1.9	78 ± 8	9.7 ± 0.1 s
	^{202}At	6154 ± 18	6227.7 ± 1.4	37 ^a	3.07 ± 0.02 min

obtained from Ref. [29].

^aUncertainty not reported.

TABLE III. List of all EvR cross sections reported in this work. $E_{\text{Lab, CoT}}$ is the lab-frame projectile energy in the center of the target. Asymmetric errors bars are reported for data points with low statistics. Some of these data are presented in Fig. 4, Fig. 5, Fig. 6, and Fig. 7.

Target	$E_{\text{Lab, CoT}}$ (MeV)	E_{CN}^* (MeV)	σ_{3n} (μb)	σ_{4n} (μb)	σ_{5n} (μb)	σ_{6n} (μb)	σ_{p2n} (μb)	σ_{p3n} (μb)	σ_{p4n} (μb)	σ_{p5n} (μb)
^{158}Gd	177.6	44.7	2290^{+590}_{-490}	600^{+120}_{-100}						
	184.2	49.8	910^{+340}_{-270}	1620 ± 150	200^{+60}_{-50}					
	185.7	51.0	1840^{+620}_{-480}	2100 ± 230	600^{+130}_{-110}					
	188.4	53.1	1440^{+440}_{-340}	1940 ± 190	620 ± 100					
	191.3	55.4	1020^{+360}_{-290}	1380 ± 140	1090 ± 120					
	196.0	59.1	770^{+320}_{-250}	660 ± 110	2700 ± 180	56^{+29}_{-21}				
^{159}Tb	184.7	45.8	140^{+37}_{-30}	130 ± 20						
	189.8	49.9	90^{+25}_{-21}	230 ± 20	18^{+8}_{-6}			170^{+70}_{-60}		
	196.3	54.9	23^{+11}_{-8}	120 ± 10	34^{+8}_{-7}			220^{+60}_{-50}	33^{+10}_{-8}	
	200.5	58.2		41^{+10}_{-8}	48^{+11}_{-9}			200^{+80}_{-60}	51^{+15}_{-12}	
	208.0	64.1			33^{+9}_{-7}			160^{+70}_{-50}	50^{+14}_{-11}	38^{+11}_{-9}
	183.7	43.9	71^{+17}_{-14}	50^{+13}_{-11}						
	188.9	48.0	59^{+19}_{-15}	130 ± 20				62^{+31}_{-23}		

^{162}Dy	195.4	53.1	31_{-9}^{+11}	76 ± 14	24_{-6}^{+7}	62_{-30}^{+44}	98_{-22}^{+28}	25_{-8}^{+11}	
	199.5	56.4		55_{-10}^{+12}	20_{-5}^{+7}		100_{-20}^{+30}	100 ± 20	51_{-13}^{+16}
	207.1	62.3		14_{-5}^{+7}	27_{-6}^{+7}		29_{-12}^{+17}	94 ± 18	42_{-12}^{+15}

FIGURES

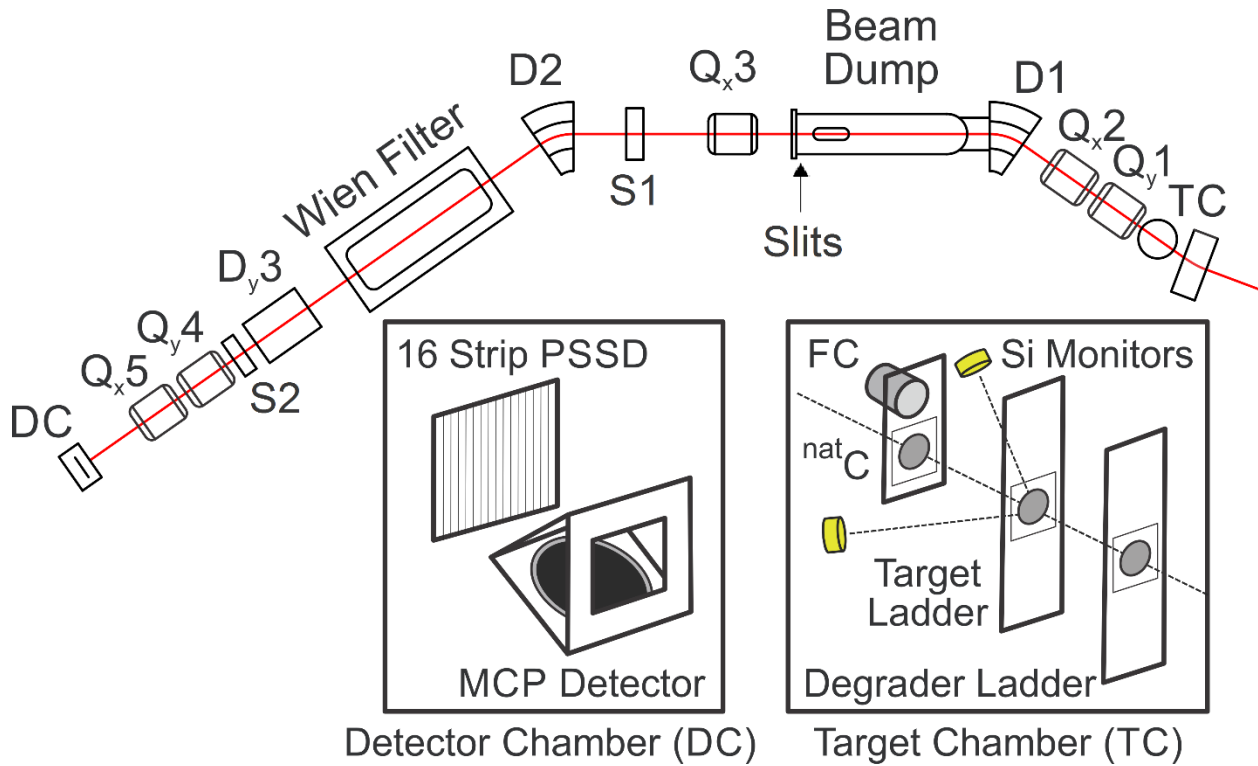


FIG. 1. (color online) MARS schematic showing the layouts of target chamber and detector chamber. The magnets labeled Q and D indicate quadrupole and dipole magnets, respectively, with the subscript and/or number denoting the focusing plane and downstream position of each magnet. S1 and S2 are sextupole magnets. The Slits define the momentum acceptance.

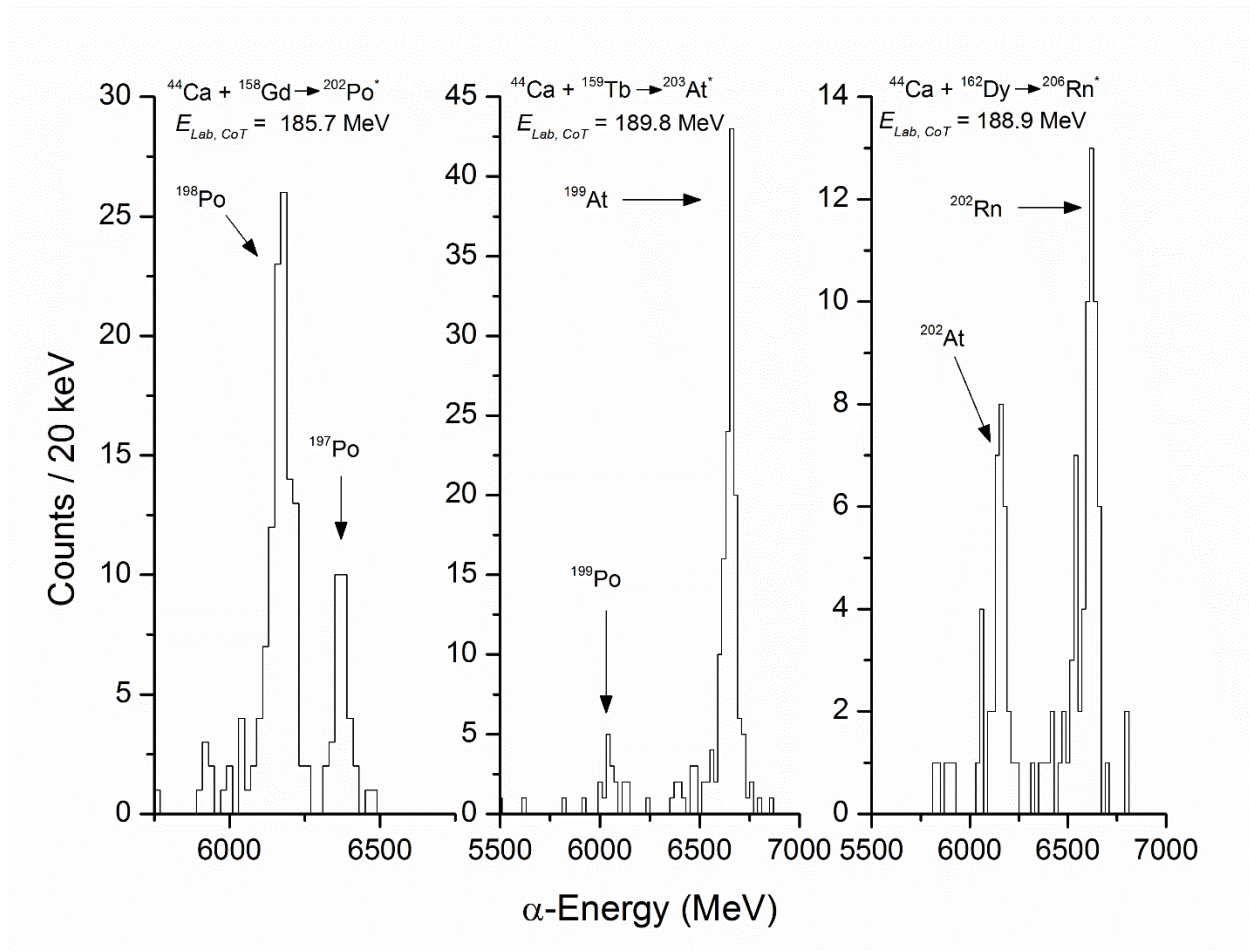


FIG 2. Representative alpha spectra observed in the ^{44}Ca -induced reactions studied in this work. The indicated center-of-target lab frame energies, $E_{\text{Lab, CoT}}$, correspond to the peak of the $4n$ excitation functions. Arrows correspond to the expected locations of the $4n$ and either $5n$ (^{158}Gd target) or $p3n$ (^{159}Tb and ^{162}Dy targets) products.

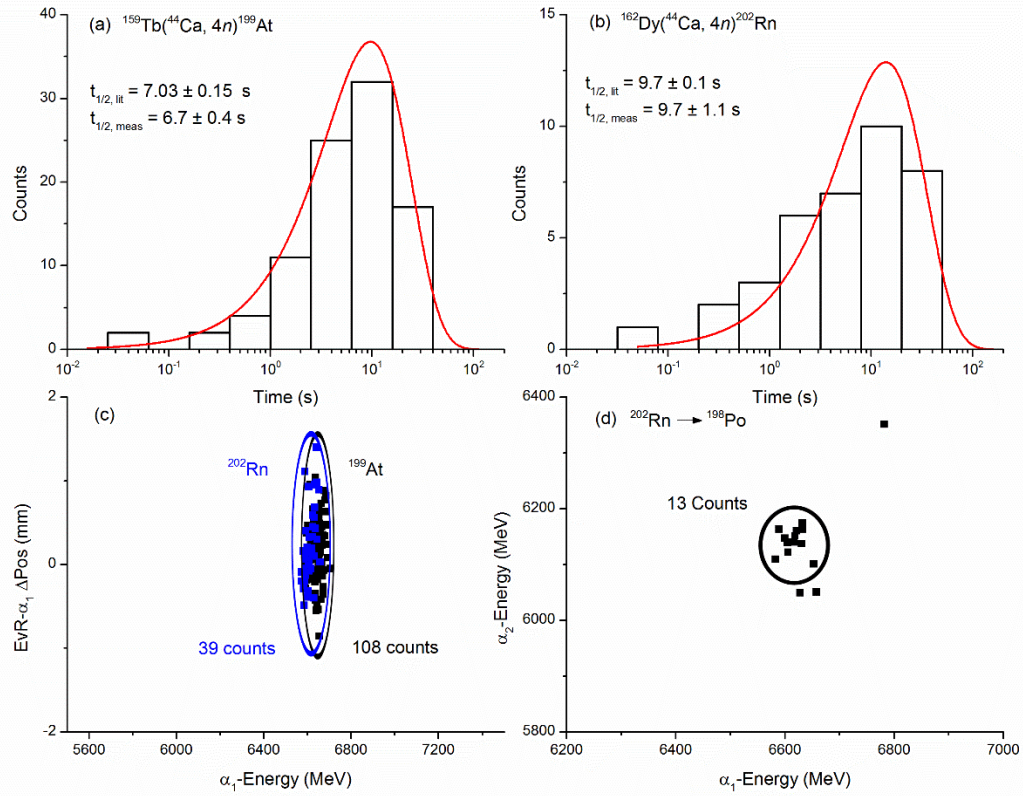


FIG. 3. (color online) EvR- α correlations for the short-lived $4n$ products of the $^{44}\text{Ca} + ^{159}\text{Tb}$ and ^{162}Dy reactions. Panels (a) and (b) are the lifetime distributions for ^{199}At and ^{202}Rn , respectively. The measured half-lives were extracted from the curves using Eq. (8) in Ref. [28] and the literature values for the half-lives were taken from Ref. [29]. The correlated EvR- α_1 position spectra are shown in (c). The parameters of the correlation search are described in the main text. The α_1 - α_2 correlation search in (d) was taken over the entire energy range shown by both axes.

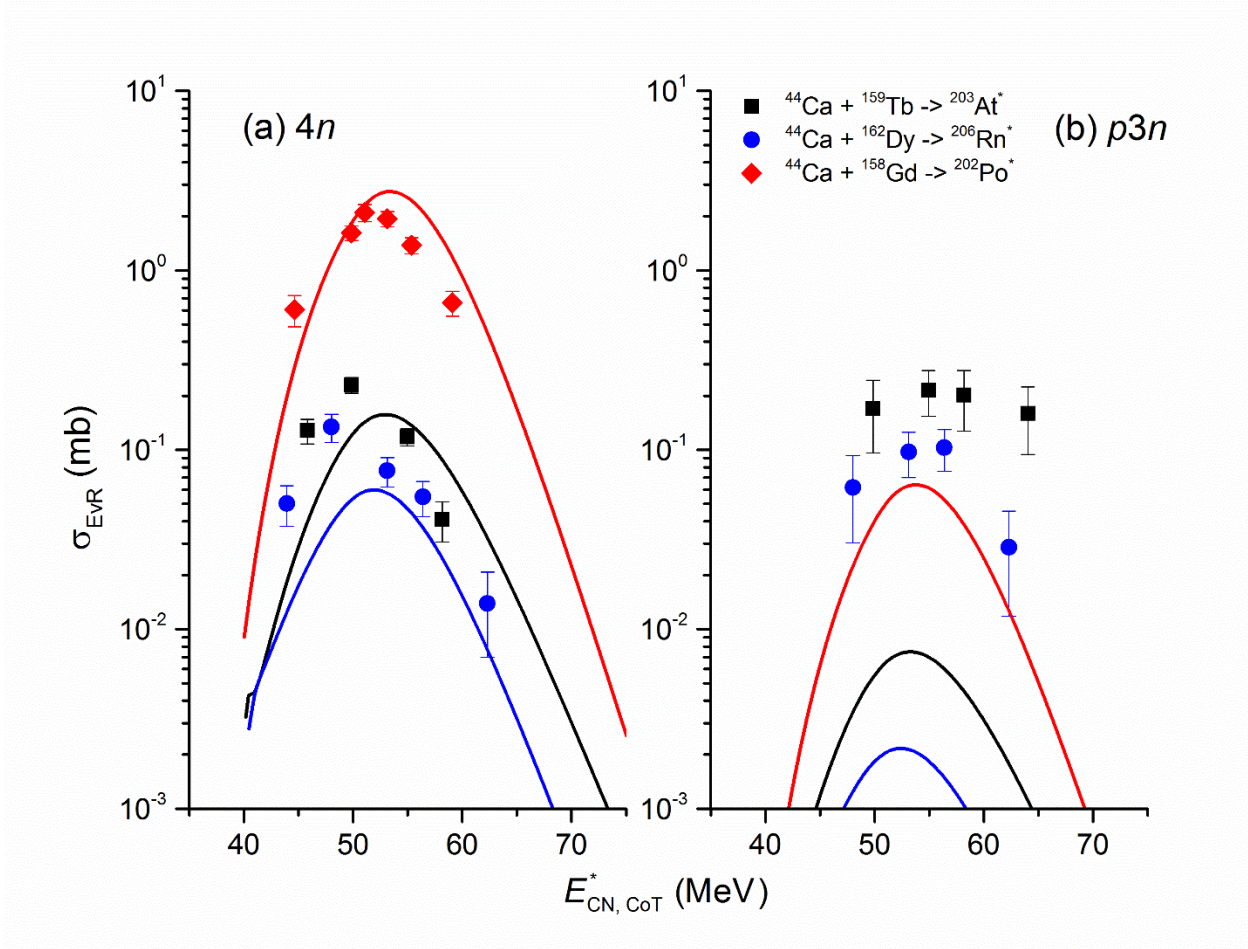


FIG 4. (color online) (a) $4n$ and (b) $p3n$ excitation functions for the ^{44}Ca -induced reactions reported in this work. Symbols represent the measured data with associated error and represent the same reactions on both panels. The solid lines are theoretical calculations using the model described in Sec. IV. The experimental data are also reported in Table III.

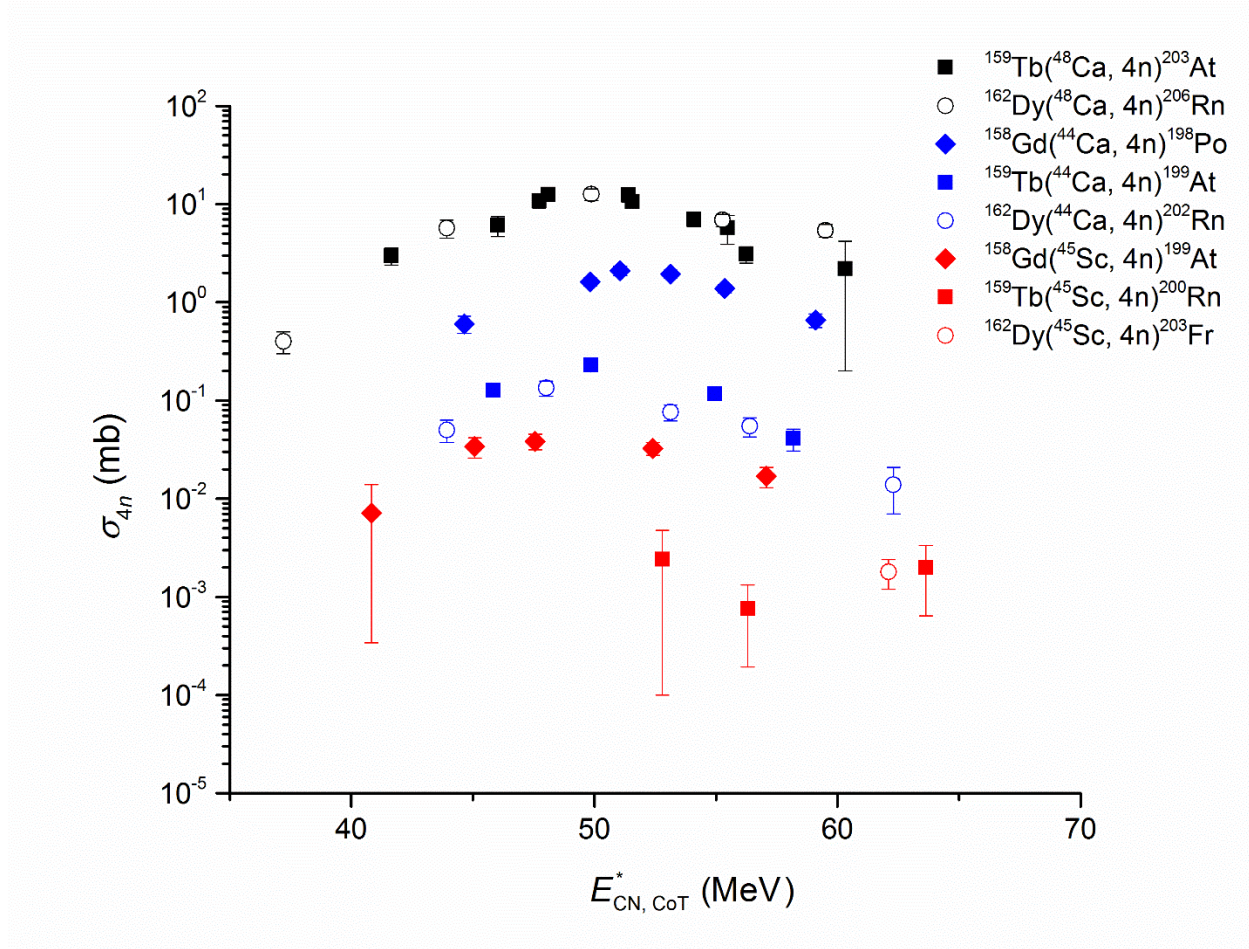


FIG. 5. (color online) Comparison of measured $4n$ cross sections of ^{48}Ca -, ^{44}Ca -, and ^{45}Sc -induced reactions on lanthanide targets. Black points represent the ^{48}Ca -induced reactions [1], blue points represent the ^{44}Ca -induced reactions (reported in this work), and red points represent the ^{45}Sc -induced reactions [3]. The shapes represent groups of reactions on the same target. Solid squares are reactions on ^{159}Tb , open circles are reactions on ^{162}Dy , and solid diamonds are reactions on ^{158}Gd . See the main text for discussion.

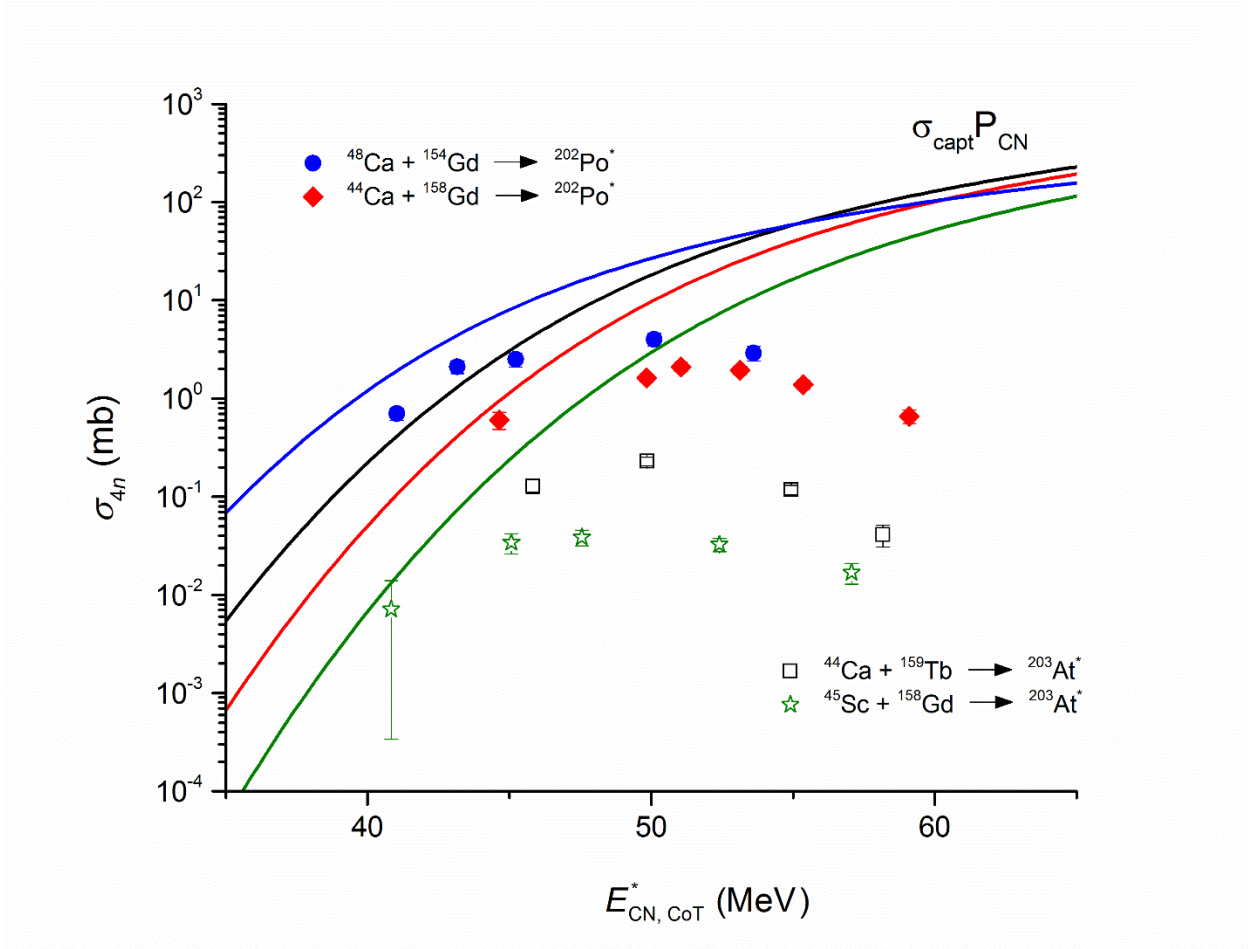


FIG 6. (color online) $4n$ EvR cross sections for the cross bombardments described in this work. Symbols are the measured data points. Solid lines represent fusion cross sections, $\sigma_{fus} = \sigma_{capt} P_{CN}$, and are calculated with the model described in Sec. IV. Each line is associated with the data points of the same color.

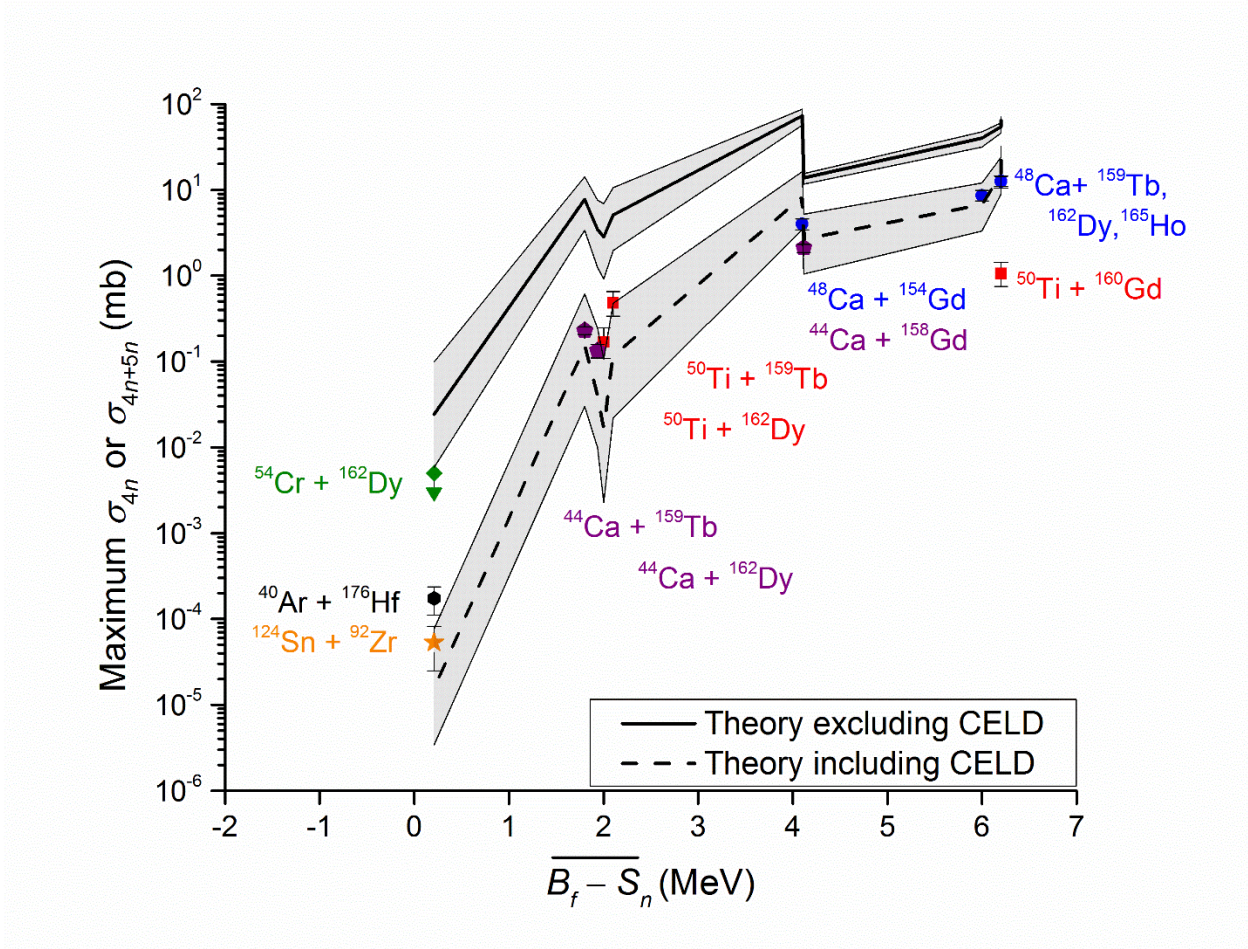


FIG 7. (color online) Maximum measured $4n$ EvR cross sections (solid symbols) as a function of the average difference in the fission barrier and the neutron separation energy during the de-excitation cascade. The ^{44}Ca data are compared to the model calculations described in Sec. IV both including (dashed line) and excluding (solid line) CELD. The model calculations for all other data are done according to the prescription in Ref. [1]. The models are identical except for the inclusion of charged-particle emission from the CN in the present work. The grey shaded regions indicate the effects of changing the fission barrier by ± 0.5 MeV. All reaction systems use even- Z projectiles and produce CN near the $N = 126$ spherical closed shell. The ^{48}Ca data are reported in [1], the ^{44}Ca data are reported in this work, the ^{50}Ti and ^{54}Cr data are reported in [2], the ^{40}Ar data are reported in [10], and the ^{124}Sn data are reported in [11]. Only upper limits were measured for the $^{54}\text{Cr} + ^{162}\text{Dy}$ reaction, and the $^{40}\text{Ar} + ^{176}\text{Hf}$ and $^{124}\text{Sn} + ^{92}\text{Zr}$ reactions are two cross bombardments that provide an estimate of $\sigma_{\max, 4n}$ for the ^{54}Cr -induced reaction.